



OPEN

Temperature dependence for high electrical performance of Mn-doped high surface area activated carbon (HSAC) as additives for hybrid capacitor

Zambaga Otgonbayar¹, Kamrun Nahar Fatema¹, Sunhye Yang^{3,4}, Ick-Jun Kim³, Minchul Kim³, Sang Eun Shim⁴✉ & Won-Chun Oh^{1,2}✉

Herein, we manufactured the positive and negative electrodes for the hybrid capacitor. The Mn-doped High surface area of Activated carbon composite used for the positive electrode and as-prepared composite was calcined at 600 °C and 800 °C. The morphological structures and pore-size distributions of MnYP-600HTT and MnYP-800HTT were characterized by means of XRD, SEM, EDAX, TEM, and BET. According to the BET specific surface-area evaluation, MnYP-600HTT and MnYP-800HTT were 1272.6 and 1388.1 m²/g, respectively. Total pore volumes were 0.627 and 0.687 cm³/g, which is beneficial for forming ion-transport channels in electrochemical reactions. The MnYP-600HTT electrode had a high specific capacity of 177.2 mAh/g at 20C, and the capacity retention was 64.8%. During the entire cycling, MnYP-600HTT had excellent cyclic stability in 500 cycles along with high efficiency. The robust design of the MnYP-600HTT and MnYP-800HTT cathode materials introduced in this work pave the way for designing next-generation supercapacitors operating at ultra-high C rates. The Mn-doped high surface of activated carbon had stable energy density and superior cycling stability that were demonstrated in supercapacitor systems.

The development of new technologies for the storage and production of electricity is a green way to prevent / reduce the environmental pollution. One of most suitable mechanism is supercapacitor, and it has the rapid charging/discharging, stable recycling performance with high rate-capability and low cost with environment friendliness¹⁻⁵.

One way to change the performance of the electrodes in a capacitor is to develop a nano-sized active material with a high surface area with particular capacitance. Carbon-based materials have been used as high-capacity electrode materials for decades^{6,7}. Some researchers synthesize carbon-based electrodes with some transition metals because of their high storage capability and unique reversibility⁸⁻¹⁰, but these kinds of materials still have some defects such as high price, inefficient electro-chemical stability and the block of the pores of carbon material that act as ion-transfer¹¹. Surface activation is the most widely used method of improving the properties of activated carbon. In addition, the creation of artificial layer on the active-material exterior to prevent any side reaction mechanism between the electrode and electrolyte, if this attempt is successful the result is good long-term cycling performance.

Potassium permanganate is one of the nominated reagent for the surface activation reaction¹². The role of KMnO₄ is as a surface modifier and intermediate bridge or activator for ion transfer and it is oxidizing agent that enhances the exterior functional-groups of the active material¹³. RuO₂¹⁴, NiO¹⁵, Co₃O₄^{16,17}, MnO₂¹⁸, NiCo₂O₄¹⁹, CoNiO₂²⁰, and Fe-V-O²¹ are used as cathode materials. The working potential of the cathode material is above 0 V vs. SCE and the anode material is below 0 V vs. SCE.

¹Department of Advanced Materials Science and Engineering, Hanseo University, Seosan-si, Chungnam 356-706, Republic of Korea. ²College of Materials Science and Engineering, Anhui University of Science and Technology, Huainan 232001, People's Republic of China. ³Korea Electrotechnology Research Institute, 12, Boolmosan-ro, 10beon-gil, Seongsan-gu, Changwon-si, Gyeongsangnam-do 51543, Republic of Korea. ⁴Department of Chemical Engineering, Inha University, 100 Inha-ro, Michuhol-gu, Incheon 22212, Republic of Korea. ✉email: seshim@inha.ac.kr; wc_oh@hanseo.ac.kr

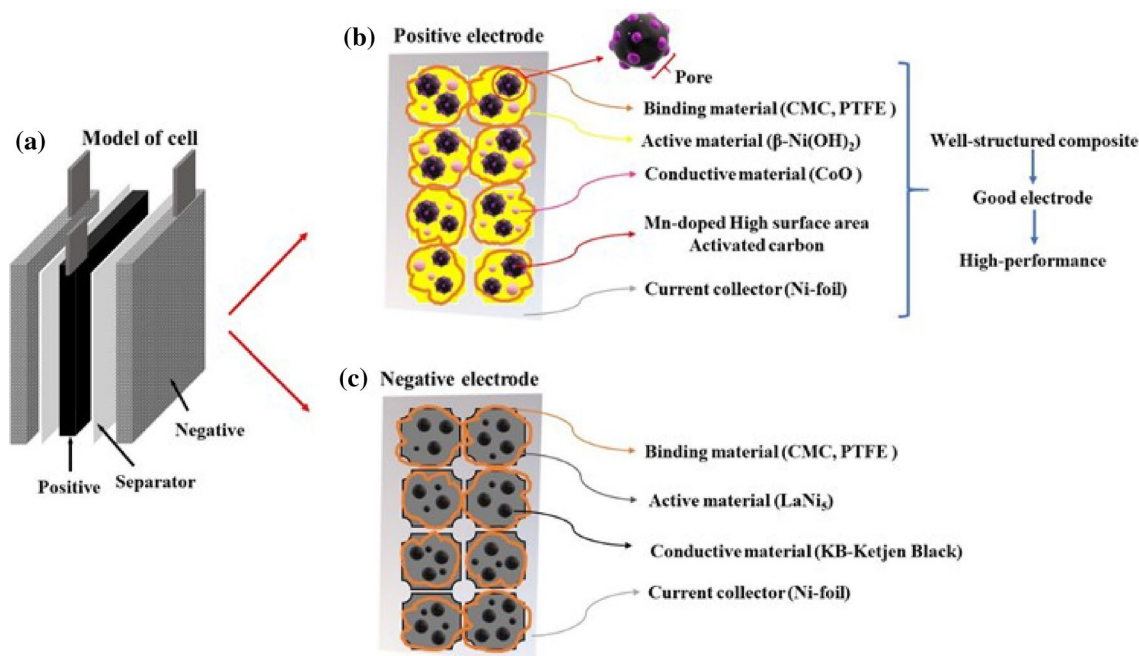


Figure 1. (a) Schematic illustration of the model of the Ni-hybrid capacitor, (b) detailed structure of the positive electrode, (c) detailed structure of the negative electrode.

Mn-treated activated carbon and graphene were studied for the anode material in capacitor. Such as, $\text{Mn}_3\text{O}_4/3\text{D-graphene}$ as positive electrode²², Mn-doped $\text{Fe}_2\text{O}_3@\text{rGO}$ NPs as anode²³, $\text{LiMn}_2\text{O}_4@\text{CNTs@graphene}$ composite for cathode for aqueous hybrid capacitors²⁴ and Mn-doped ZnS nanosheets (ZnS:Mn NS) as the positive²⁵. Mn-treated active material had high specific capacitance and excellent cycling profile.

In this regard, Mn-doped HSAC composites were used for the positive electrode and LaNi_5 was used for the negative electrode. Mn-doped HSAC composites were calcined at 600 °C and 800 °C. As-prepared MnYP-600HTT and MnYP-800HTT cathode electrodes proved to have an exceptional electrochemical performance, with a specific surface area of 1272.6 and 1388.1 m^2/g , a specific capacity of 294.7 mAh g^{-1} of the charging state, and 258.4 and 246.1 mAh g^{-1} of the discharging state in the Charge/Discharge profile after 10 cycles. A Mn-doped HSAC two-cathode electrode had good stability under a 500-cycle test. Those results are higher than those of pure pristine, which confirms that MnYP-600HTT and MnYP-800HTT electrodes are stable under long-time cycles. By comparing these three cycling performance curves, it can be seen that there is a process of activating capacity that happens during the initial cycles. This approach presented herein offers a promising route for the rational design of a new class of supercapacitors.

Experiment part

Preparation of Mn-doped high surface area Activated carbon (HSAC). 1 g of pure pristine diffused into as-prepared 1.5 M of HCl, HNO_3 and H_2SO_4 acidic-solvent. The solution was mixed for 6 h and this was followed by a vaporization process. The mixture transferred into oven and dried at 110 °C for 8 h until it turns into a powder. Then acid-treated powder dispersed into 0.5 M concentrated sub-active reagent solution and stirred for 2 h at 80 °C to create a chemical bond between the sub-active material and activated carbon. Finally, the composite dried at 100 °C to obtain a powder and then calcined at 600 °C for 2 h for purification and to improve their surface properties.

Anode manufacturing method. A positive electrode was prepared using $\beta\text{-Ni}(\text{OH})_2$, a conductive material CoO (Alfa Aesar), a binder CMC (Carboxymethyl cellulose), and PTFE (Polytetrafluoroethylene), and the electrode composition was 95:1:2:2 wt%. In the electrode manufacturing process, binders CMC (Carboxymethyl cellulose) and PTFE (Polytetrafluoroethylene) were dispersed in DI-water, and then $\beta\text{-Ni}(\text{OH})_2$ and CoO were added to prepare a slurry electrode using a mixer (Thinky mixer). The electrode slurry to which the activated carbon additive was applied was added in 10 wt% of the active material to prepare a slurry electrode. The slurry electrode thus prepared was coated on a Ni-foam type current collector by applying a dip coating process, dried in a 100 °C oven, and pressed to a thickness of 300 μm using a roll press equipment. The schematic illustration of the anode was displayed in Fig. 1.

Cathode manufacturing method. A negative electrode was manufactured using LaNi_5 , a conductive material KB (Ketjen Black), a binder CMC (Carboxymethyl cellulose), and PTFE (Polytetrafluoroethylene), and the electrode composition was 93:4:2:1 wt%. In the electrode manufacturing process, binders CMC (Carboxymethyl cellulose) and PTFE (Polytetrafluoroethylene) were dispersed in DI-water, and LaNi_5 and KB were added

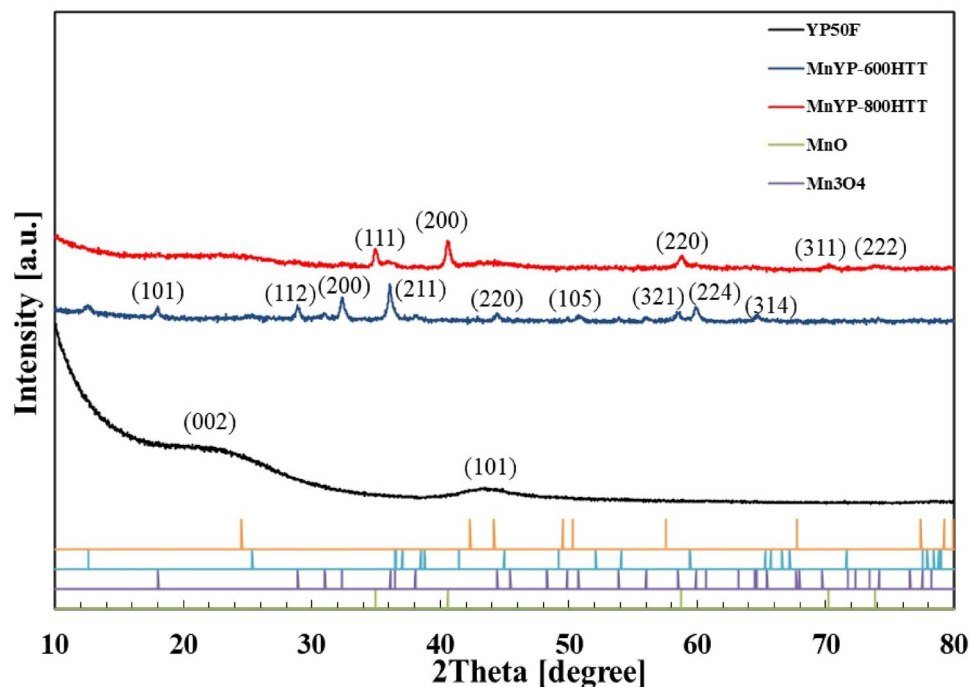


Figure 2. XRD pattern of Mn-doped MnYP-600HTT and MnYP-800HTT.

to prepare a slurry electrode using a mixer (Thinky mixer). The slurry electrode thus prepared was coated on a Ni-foam type current collector by applying a dip coating process, dried in a 100 °C oven, and pressed to a thickness of 250 μm using a roll press equipment. The schematic illustration of the cathode was displayed in Fig. 1.

Cell manufacturing process. We prepared an electrode with a capacity ratio of 1:2.5 of the positive electrode and the negative electrode. A separator was placed between the two negative electrodes, and the positive electrode was placed in the middle to prepare a cell. We impregnated it with 10 g of 6 M KOH and 0.3 M LiOH in distilled deionized (DDI) water and kept it under vacuum for 12 h, followed by a cell test.

Characterization. The crystalline structure was examined by X-ray diffraction instrument (SHIMADZU XRD-6000) with 1°/min scan rate. The morphology of the KMnO₄-HSACs were analysed using SEM/TEM and HRTEM (JSM-5600 JEOL, Japan) (TEM, Hitachi HT7700, operated at 100 kV). The presence of the elements was analysed via EDX analysis conducted into SEM. The surface chemical state of material was analysed via X-ray photoelectron spectra (KRATOS AXIS SUPRA).

Electrochemical test. To form a nickel hybrid capacitor cell with electrolyte aging completed, it was charged with a constant current of 0.1C and discharged to 1.0 V at a constant current of 0.1C, which was done for 10 cycles. After cell formation was complete, we measured a Nyquist plot at a frequency range of 1–1 MHz and an amplitude of 10 mV for EIS (Electrochemical Impedance Spectroscopy) analysis. To evaluate the output characteristics according to the current of the cell, we did a rate capability test in the current range of 0.2–30 C, with the cell being charged and discharged up to 500 cycles at a constant current of 1C.

Result and discussion

X-ray diffraction studies and morphological characterization. The XRD pattern of Mn-doped activated carbon after heat treatment at 600 and 800 °C is shown in Fig. 2. We ascribed the peaks to the presence of MnO in Mn-YP800HTT. Diffraction peaks at 2θ of 34.9, 40.6, 58.8, 70.3, and 73.8 were ascribed to the crystalline planes (111), (200), (220), (311), and (222), respectively, of MnO (JCPDS No. 89-4835) to confirm the presence of Mn on the activated carbon surface. For Mn-YP600HTT, all peaks showed the presence of Mn₃O₄. The diffraction peaks were ascribed to the crystalline planes (112), (103), (211), (004), (220), and (224) of Mn₃O₄ (JCPDS Card No.00-001-1127). According to the XRD result, the temperature difference can affect the crystal structure of Mn.

The quantitative as well as qualitative number of the main elements in the catalyst were detected via EDX analysis, which also revealed each element's characteristic peak (sharp K_α and K_β). Figure 3 displays the micro-analysis results of all as-synthesized samples; it shows the presence of the main elements. K, Mn, and O come from the doping reagent, whereas C comes from the activated carbon. According to the EDAX analysis, a small amount of Al and Cl were detected. In addition, the amount of Mn was not the same, because of temperature dependency.

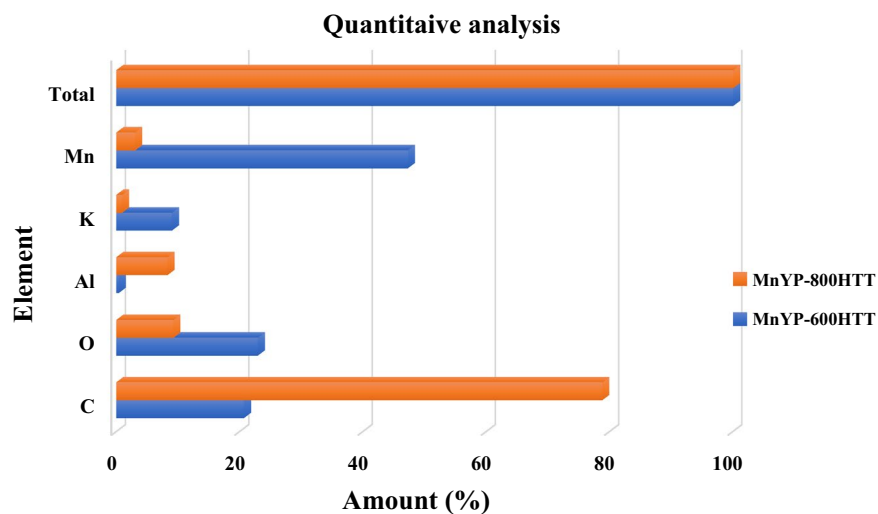
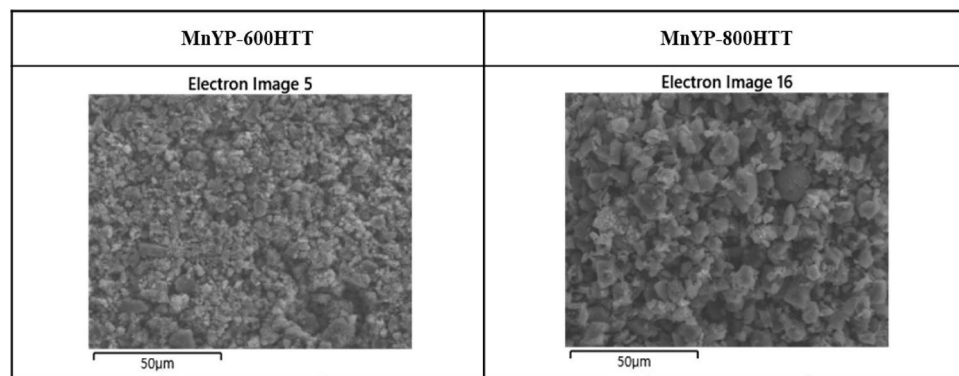


Figure 3. The quantitative analysis results.

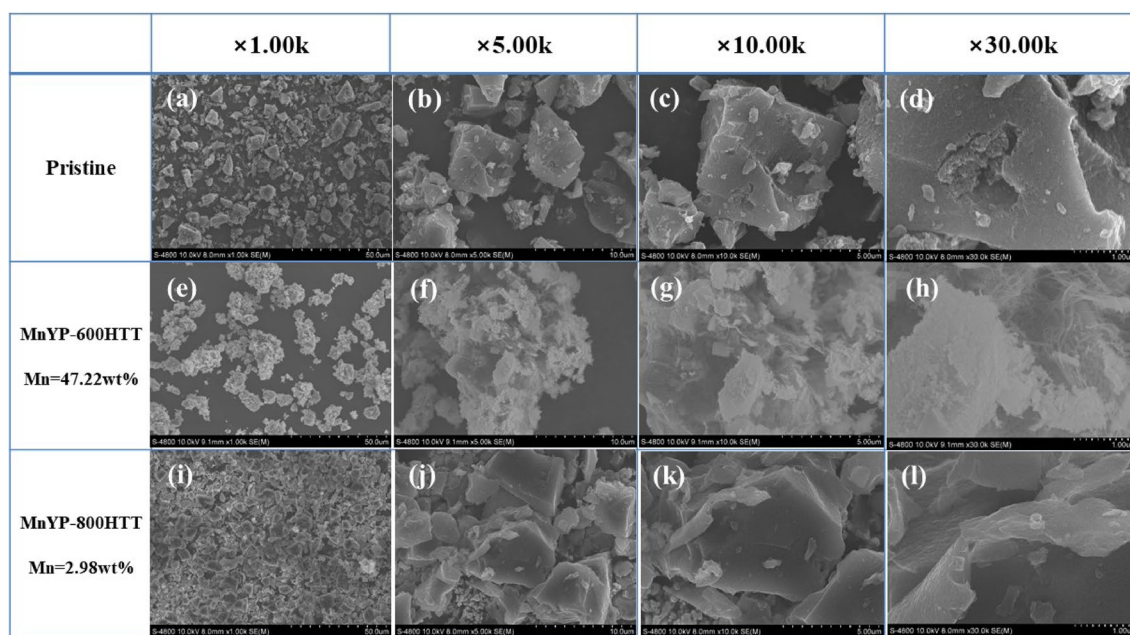


Figure 4. SEM images of Pristine, Mn-doped MnYP-600HTT and MnYP-800HTT.

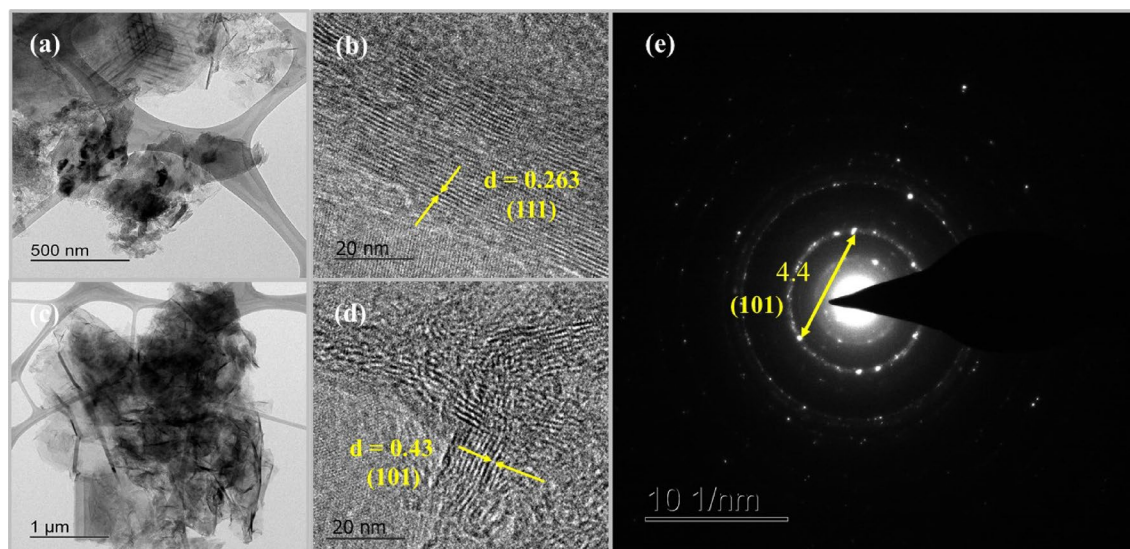


Figure 5. (a–d) TEM and HRTEM images of Pristine, Mn-doped MnYP-600HTT and MnYP-800HTT, (e) SAED pattern of Mn-doped HSAC.

We investigated the surface morphology with SEM. Figure 4 shows the SEM analysis results of the Mn-doped high surface area of activated carbon after 600 °C and 800 °C calcination. The pure pristine had several structures of particles, as shown in Fig. 4a–d. From the image, it can be seen that the Mn particles fully covered the surface of activated carbon in MnYP-600HTT. The morphology of MnYP-600HTT was web-shaped, as shown in Fig. 4e–h. For MnYP-800HTT, the surface of each particle was smooth and covered by Mn. All particles are gathered in Fig. 4i–l. The amount of Mn was not the same in each prepared sample, which can affect the surface and property of a composite material. The main role of the large surface area of the pristine is to provide a sufficient area of the nanocomposite that can be grown on the surface during synthesis. In addition, the graphene made a chemical bond with precursor reagents by means of oxygen-containing functional groups. Furthermore, the results of SEM showed the distinction between the Mn-doped HSAC composite under the 600 °C and that under 800 °C.

The atomic structure and information of crystallographic structure of nanocomposite was analyzed via HRTEM. Figure 5a,c shows the TEM images of Mn-doped HSAC which exhibited that Mn-particles had irregular shape and all materials is enveloped in high surface area of activated carbon, resulting in a good composite. Figure 5b,d indicated the lattice fringes of Mn-doped HSAC composite under the 600 °C and that under 800 °C. The lattice fringes with d-spacing of Mn-doped HSAC was 0.263 and 0.43 nm and these are corresponding to the (111) and (101) crystal planes of MnO and Mn₃O₄, respectively. The selected area electron diffraction (SAED) was used to fully reconstruct the reciprocal space. Figure 5e shows the (101) zone axis and width was 4.4 nm which can be indexed on the basis of a Mn₃O₄.

The specific surface area, pore diameter, and pore volume affect the electrochemical properties. Figure 6 shows the N₂-adsorption-desorption isotherm of MnYP-600HTT and MnYP-800HTT composites. BET and BJH method used for the analysis of specific surface area and pore-size distribution. The calculation results were summarized in Table 1. The relative pressure is (0.5–1.0) P/P₀, as shown in Fig. 6. According from Fig. 6, relation between pore-distribution and isotherm belonged to the H1, this result can confirm the all composites has slender pore-size. The isotherm type IV is characteristic of mesoporous/micropores adsorbents. The specific surface area of pure pristine was 1676.1 m²g⁻¹, and the average pore diameter was 1.85 nm. After the synthesis, the specific surface area and mean pore diameter were increased in MnYP-800HTT. According to the calculated T-plot, the total surface area was high in pristine. After Mn-dope and calcination, the surface area decreased, but MnYP-800HTT still had a larger surface area than did MnYP-600HTT. The total specific surface area of MnYP-600HTT was 1412.6 m²/g, whereas MnYP-800HTT had 1578.6 m²/g. Micropore volume was decreased from 0.693 to 0.567 cm³/g, and mesopore volume increased from 0.084 to 0.120 cm³/g in the MnYP-800HTT sample, which is beneficial for forming ion-transport channels in electrochemical reactions.

To explore the detailed surface chemical state of the elements and interactions between Mn and HSAC, we did an XPS analysis of Mn-doped HSAC. The binding energies depend on the chemical structure and elemental formation of the sample. Figure 7a presents the XPS survey spectrum, which shows the existence of C1s, O1s, Mn, and K, thus confirming the successful formation of Mn-doped activated carbon. Figure 7b shows the C1s XPS spectrum, which consists of some characteristic peaks, such as carbonyl carbon (C=O, 288.4–288.6 eV), aliphatic (C–C, 284.4–285.9 eV) and carboxylate carbon (O–C=O, 289.3 eV)²⁶. These peaks corresponded to the state of carbon with carbon bonded by a single bond (C–C) and the state of carbon linked by a single bond to an oxygen-containing group (C–O(O)). The C1s XPS shows five notable peaks corresponding to non-oxygenated carbon (285.24 eV) and carboxylate group (291.22 eV)²⁷. Figure 7c shows the O1s spectra on graphene and Mn. The peak location relates to the functional group, such as, the O1s peak located at over 531 eV region express the metal-oxide group, if it is below 531 eV can express the carbonyl or hydroxide group²⁸. In the XPS spectrum of O1s, the broad peak was located at 531.16 eV, which indicated the carbonyl group. In addition, The second-peak which located at 553.86 eV expresses the chemical interaction between metal (X) and oxygen. The electronic

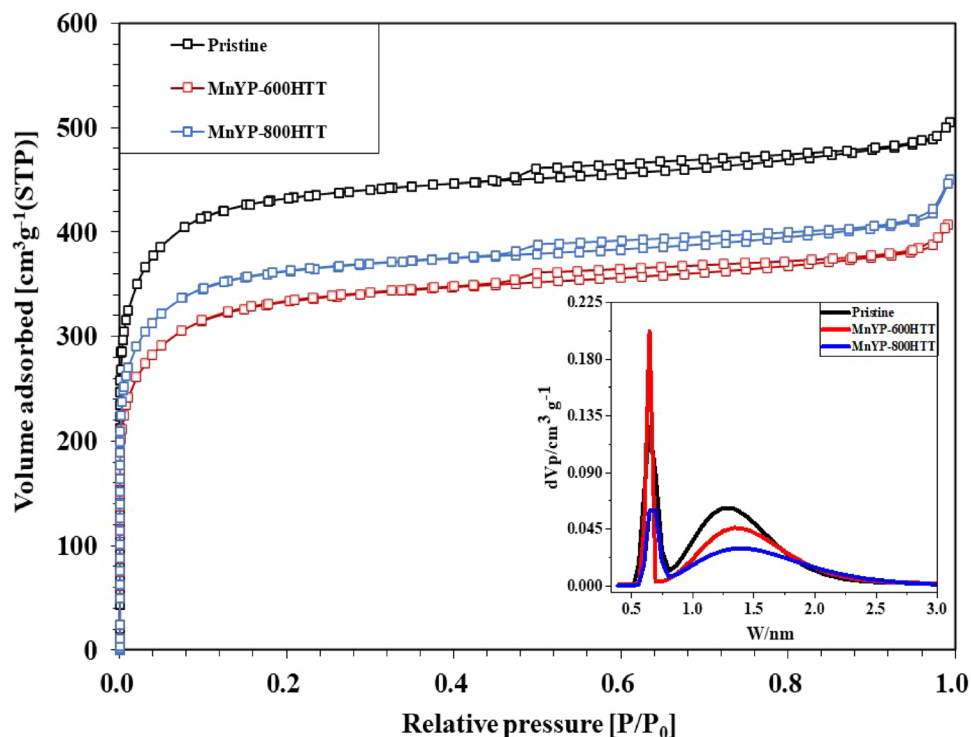


Figure 6. Nitrogen adsorption–desorption isotherms of Pristine, Mn-doped MnYP-600HTT and MnYP-800HTT.

Mn-doped A.C. additives	Pore structure parameter								
	BET			T-plot					
	Surface area (m ² /g)	Total pore volume (cm ³ /g)	Mean pore diameter (nm)	Total surface area (m ² /g)	Micropore surface area (m ² /g)	External surface (m ² /g)	Micropore volume (cm ³ /g)	Mesopore volume (cm ³ /g)	Micropore vol. percent (%)
Pristine	1676.1	0.776	1.85	1898.4	1639.4	36.7	0.693	0.084	89
MnYP-600HTT	1272.6	0.627	1.97	1412.6	1236.6	36.0	0.534	0.093	85
MnYP-800HTT	1388.1	0.687	1.98	1578.6	1344.4	43.7	0.567	0.120	83

Table 1. Nitrogen adsorption–desorption isotherms of Pristine, Mn-doped MnYP-600HTT and MnYP-800HTT.

configuration of Mn2p is shown in two peaks, which correspond to the mixed valence state, as shown in Fig. 7d. Mn 2p_{1/2} is located at the 666.23 eV binding energy region, and the Mn 2p_{3/2} peak can be deconvoluted into two peaks of 30.34% Mn³⁺ (643.32 eV), and 29.54% Mn⁴⁺ (647.28 eV), corresponding to the spin–orbit peaks of Mn with mixed valence states of +3 and +4, respectively²⁹. The binding energy shifts indicate the strong bond–interaction and charge transfer between the Mn and HSAC.

Electrochemical evaluation. Figure 8 presents the charge–discharge profiles of pure pristine and MnYP-800HTT. The negative electrode was LaNi₅ and the as-prepared samples were the positive electrode under the applied current. The charge–discharge profiles experiment was Super charging at 0.01C, 0.02C, 0.05C × 5 h (Cut-off time); Super discharge at 0.05C to 1.0 V (Cut-off voltage); Charging at 0.1C × 12 h (120% charging); and discharging at 0.1C MnYP-600HTT, 1.0 V (Cut-off voltage). During a ten-cycling test, all samples had high capacity, and MnYP-800HTT showed quite a different charge–discharge profile because of the amount of Mn and specific surface area. According to the EDAX analysis, the amount of Mn in MnYP-800HTT was 2.98% and specific surface area and total surface area were higher than in MnYP-600HTT, which was close to pure pristine. Moreover, the MnYP-600HTT electrode has an obvious charging platform, and the charging characteristics of the MnYP-600HTT and MnYP-800HTT electrodes are more consistent with similar capacitance characteristics.

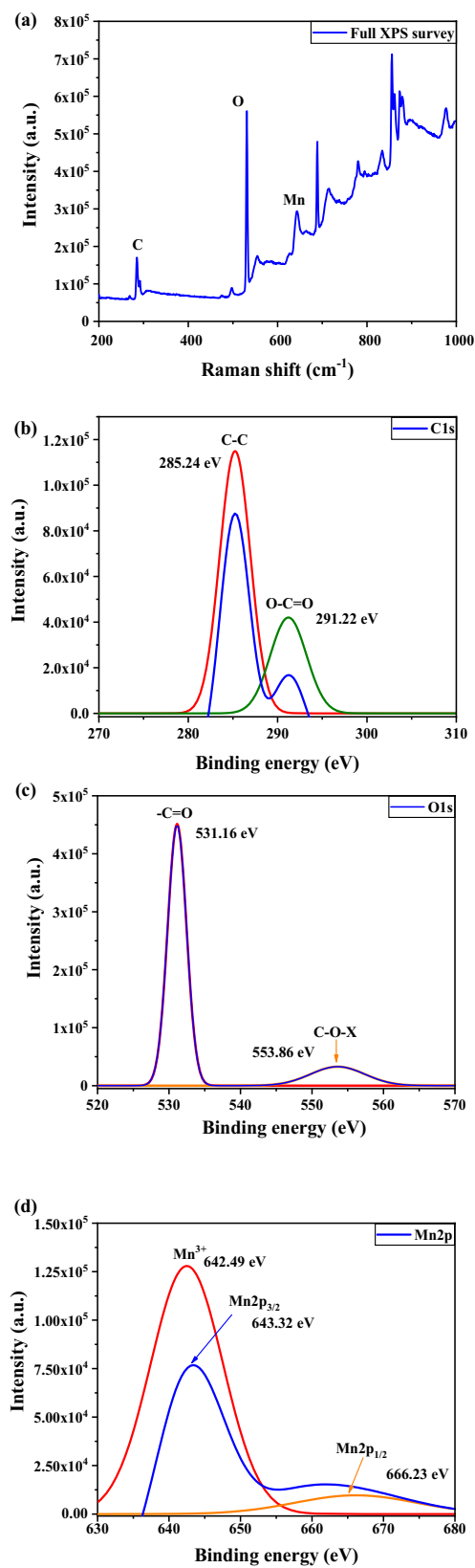


Figure 7. Survey XPS spectrum (a) and high-resolution XPS spectra of (b) C1s, (c) O1s, (d) Mn2p.

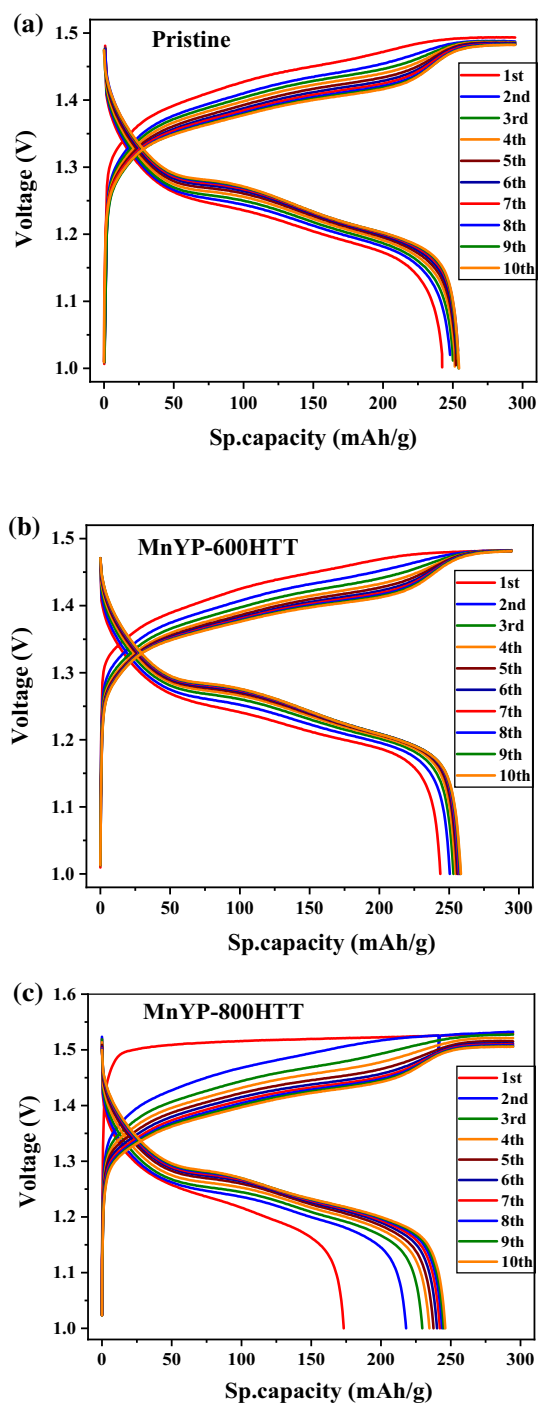


Figure 8. The charge–discharge profiles of Pristine, Mn-doped MnYP-600HTT, MnYP-800HTT.

Figure 9 shows the charge–discharge profiles of the hybrid device composed with LaNi_5 as the negative electrode and the pristine, MnYP-600HTT, and MnYP-800HTT as the positive electrode under an applied current of state. The experiment was a charge/discharge test (10 cycles): Charging $0.2\text{C} \times 6\text{ h}$ (cut-off time, 120% charging); Discharge 0.2C , 1.0 V (Cut-off voltage). The specific capacity of the positive electrode is calculated in Fig. 9. In the charge state, the amounts of capacity [mAh] of each positive electrode were 94.9 mAh in Pristine, 93.4 mAh in MnYP-600HTT, and 80.0 mAh in MnYP-800HTT. In the charged state, the capacities of Pristine, MnYP-600HTT, and MnYP-800HTT were 94.9, 93.4, and 80.8 mAh. The capacities were 81.9, 81.9, and 66.8 mAh in the discharged state. The specific capacities of Pristine, MnYP-600HTT, and MnYP-800HTT were equal to each other, at around 294.7 mAh/g . Specific capacities were 254.5 , 258.4 , and 246.1 mAh/g in the discharged state. The ultra-specific capacity was successfully demonstrated in MnYP-600HTT. The charging and discharging capacity

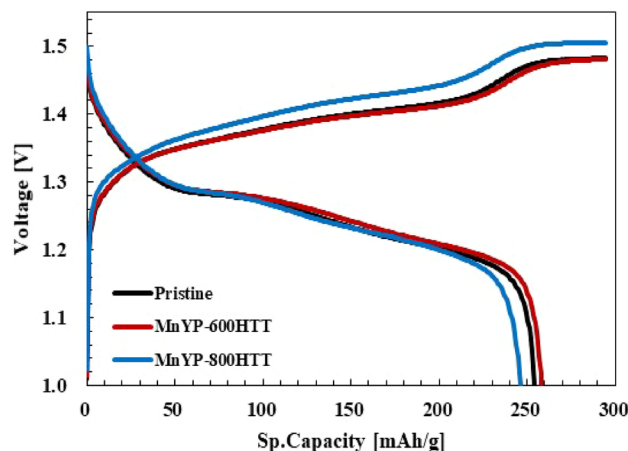


Figure 9. The charge–discharge profiles of Pristine, Mn-doped MnYP-600HTT and MnYP-800HTT after 10 cycles.

Positive	Negative	Charge		Discharge	
		Capacity (mAh)	Sp. capacity (mAh/g)	Capacity (mAh)	Sp. capacity (mAh/g)
Pristine	LaNi ₃	94.9	294.7	81.9	254.5
MnYP-600HTT	LaNi ₃	93.4	294.7	81.9	258.4
MnYP-800HTT	LaNi ₃	80.0	294.7	66.8	246.1

Table 2. A table for comparison between Mn-doped carbon materials for supercapacitor.

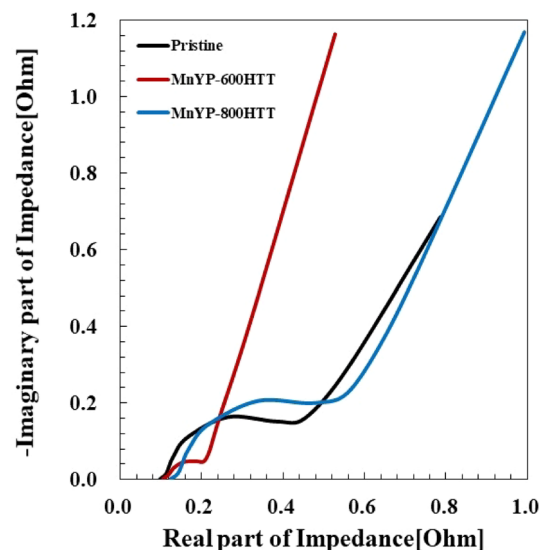


Figure 10. Nyquist plot of Pristine, Mn-doped MnYP-600HTT and MnYP-800HTT.

and specific capacity of MnYP-800HTT were less than those of the other two samples. A table for comparison between the Mn-doped carbon materials for supercapacitors is given in Table 2.

Figure 10 shows the Nyquist plots of the electrodes, displaying two depressed semicircles within the frequency range of 1–1 MHz and 10 mv of amplitude. Theoretically, the first depressed semicircle (under high frequency) may be related to the Mn⁺ displacement passing through the electrode and the next semicircle related to the charge transfer between electrode/electrolyte. Lastly the Mn ions may diffuse on the electrodes under the low frequency condition. The real axis state and semicircle profile can relate to the resistivity of the electrolyte, interaction between active material and current-collector, charge transfer property. The deviation of the pristine and MnYP-800HTT was around 40% MnYP-600HTT was 20% in the 0.1–1.0 Ω impedance range. As can be shown in Fig. 10, we measured Rs of 0.70, 1.16, and 1.17 Ω for pure pristine, Mn-doped MnYP-600HTT, and Mn-doped

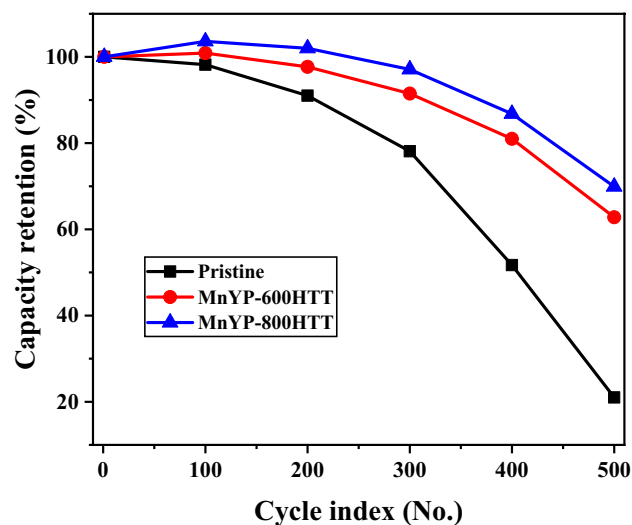


Figure 11. Cycling test of Pristine, Mn-doped MnYP-600HTT and MnYP-800HTT under 500 cycles.

Mn-doped A.C. additives	Cycle index (no.)					
	1st	100th	200th	300th	400th	500th
Pristine						
Capacity (mAh)	82.1	80.6	74.7	64.1	42.4	17.3
Sp.Capacity (mAh/g)	261.1	256.4	237.5	204.0	134.9	54.9
Capacity retention (%)	100.0	98.2	91.0	78.1	51.7	21.0
MnYP-600HTT						
Capacity (mAh)	83.2	84.0	81.3	76.2	67.4	52.3
Sp.Capacity (mAh/g)	262.8	265.2	256.7	240.5	212.8	165.0
Capacity retention (%)	100.0	100.9	97.7	91.5	81.0	62.8
MnYP-800HTT						
Capacity (mAh)	62.7	64.9	64.0	60.9	54.4	43.9
Sp.Capacity (mAh/g)	231.1	239.4	235.8	224.5	200.7	161.6
Capacity retention (%)	100.0	103.6	102.0	97.1	86.8	69.9

Table 3. Cycling test result of Pristine, Mn-doped MnYP-600HTT and MnYP-800HTT under 500 cycles.

MnYP-800HTT electrodes, respectively. The Mn-doped MnYP-600HTT nanocomposite shows lower R_s than does the Mn-doped MnYP-800HTT nanocomposite, attributed to the doping effect by Mn in the MnYP-600HTT and MnYP-800HTT nanocomposite. Lower resistance confirmed that the sample has a high conductive property. Comparing the EIS of the three cases, MnYP-600HTT and MnYP-800HTT had a significant slope on the Y axis in the low-frequency region due to the easy absorption/reception of electrode ions. Furthermore, in the low-frequency region, the EIS of Mn-doped MnYP-600HTT is even more inclined to the imaginary axis than is the Mn-doped MnYP-800HTT, indicating that Mn doping in the electrodes promotes the formation of a more effective channel, which is more conducive for the ion diffusion.

We tested the cycling stability of pure pristine, Mn-doped MnYP-600HTT, and Mn-doped MnYP-800HTT electrodes by using GCD measurements at 1 V for 500 cycles, as shown in Fig. 11. The values of capacitance retention for pure pristine, Mn-doped MnYP-600HTT, and Mn-doped MnYP-800HTT electrodes were 100% of the maximum capacitance at the first cycle. After the 500th cycling test, the Mn-doped MnYP-600HTT and Mn-doped MnYP-800HTT electrodes were at 62.8 and 69.9% of the 52.3 and 43.9 mAh capacity. Those results are higher than for pure pristine, which confirms that Mn-doped MnYP-600HTT and MnYP-800HTT electrodes are stable under long-time cycles.

The activation process happens in the initial recycling step and the activation time depend on the active material. Mn-doped electrode required a long activation time due to recrystallization. Above mentioned factor affects the decay-time of MnYP-600HTT and MnYP-800HTT in the charge/discharge cycles. Clearly, Mn-doped MnYP-600HTT and MnYP-800HTT can achieve both relatively high specific capacity and good cycling behavior, simultaneously. The specific capacity of Mn-doped MnYP-600HTT was 262.8 mAh/g, and Mn-doped

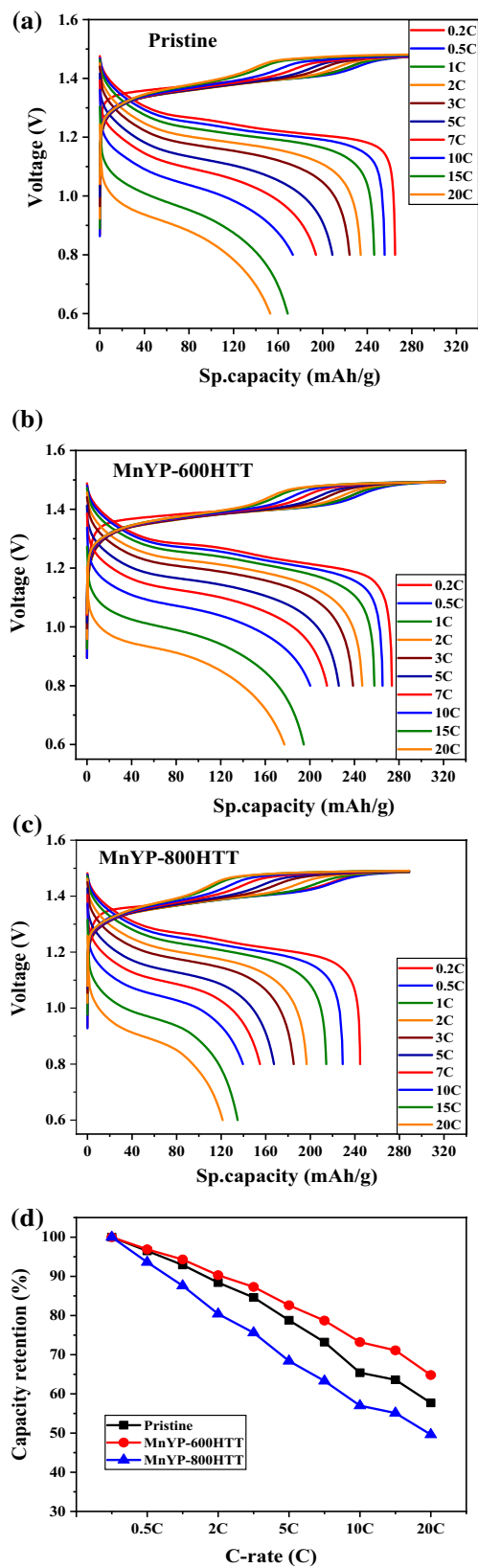


Figure 12. Rate capability test of Pristine, Mn-doped MnYP-600HTT and MnYP-800HTT under different C.

Mn-doped A.C. additives	C-rate (C)									
	0.2C	0.5C	1C	2C	3C	5C	7C	10C	15C	20C
Pristine										
Sp. capacity (mAh/g)	265.0	255.6	246.2	234.1	224.2	208.7	194.0	173.2	168.6	152.9
Capacity retention (%)	100.0	96.5	92.9	88.4	84.6	78.8	73.2	65.4	63.6	57.7
MnYP-600HTT										
Sp. capacity (mAh/g)	273.6	265.2	257.9	247.0	238.7	225.9	215.4	200.3	194.5	177.2
Capacity retention (%)	100.0	96.9	94.3	90.3	87.3	82.6	78.7	73.2	71.1	64.8
MnYP-800HTT										
Sp. capacity (mAh/g)	244.7	229.1	214.3	196.7	185.1	167.4	154.8	139.5	134.8	121.3
Capacity retention (%)	100.0	93.6	87.6	80.4	75.6	68.4	63.3	57.0	55.1	49.6

Table 4. Rate capability property of Pristine, Mn-doped MnYP-600HTT and MnYP-800HTT under different C.

MnYP-800HTT had 231.1 mAh/g at the 1st cycle. After the 500th cycle, the specific capacities were decreased to 165.0 and 161.6 mAh/g, respectively. The capacity, specific capacitance, and capacity retention (%) of all samples are summarized in Table 3. More specifically, Mn-doped HSAC materials exhibited a high specific capacitance, and the loss of specific capacities was around 37.21% and 30.07% in each Mn-doped sample. In addition to such a high mass loading, high specific capacity and good cycle performance were also achieved, indicating that our method is feasible for practical application of the positive electrode materials in a supercapacitor.

The rate capability performance was conducted for the Mn-doped HSAC cathode electrode. As shown in Fig. 12, the Mn-doped MnYP-600HTT cathode electrodes outperformed the pure Pristine electrode at various cycling conditions. The peaks were obtained in the 0.6–1.5 voltage region. The specific capacity of the Mn-doped HSAC cathode electrode is calculated in Fig. 12. The specific capacity of the pure Pristine was 265.0 mAh/g at 0.2C and decreased to 152.9 mAh/g at 20C. For the MnYP-600HTT, MnYP-800HTT had 273.7 mAh/g and 244.7 mAh/g. This result decreased to 177.2 mAh/g and 121.3 mAh/g at 20C. According to the above result, the Mn-doped MnYP-600HTT cathode had high capacity because of the amount of Mn-doping. The capacity retention of MnYP-600HTT decreased from 100 to 64.8%. The retention of MnYP-800HTT decreased from 100 to 49.6%. All results are summarized in Table 4.

All the above results confirmed that Mn-doped MnYP-600HTT electrode had a high rate capability and electrochemical property. The prominent rate capability of the Mn-doped MnYP-600HTT and MnYP-00HTT electrode can be ascribed to the unique structure, in which HSAC formed connections with Mn. The structure of the active material can upgrade the contact area between electrolyte and electrode surface, redox reaction rate. As a result, the ion-transfer performance of active-material increase in the electrochemical analysis. The total electrochemical results confirmed that a certain amount of Mn-doping under a correct calcination process can enhance the electrochemical property of HSAC materials. Furthermore, our mentioned method and results confirmed that Mn with an ultra-high surface area of activated carbon exhibited a good electrochemical property and upgraded the class of supercapacitors. Recently, some research papers reported Mn-doped graphene oxide and activated carbon for the supercapacitor, such as Mn-doped Fe₂O₃@rGO hollow core-shell spheres, MnO nanoparticles with fluorine-doped carbon³⁰, V₂O₅/polyindole (V₂O₅/PIIn) decorated onto the activated carbon³¹. Other supercapacitor materials have been studied in the field of energy storage devices, such as 3D Na₂Ti₃O₇ nanosheet arrays/carbon textiles anodes joined sodium-Ion pseudocapacitors³² NiS₂ nanosheets on porous carbon microtubes³³. The Mn-doped Fe₂O₃@rGO hollow core-shell spheres increased the active regions of redox reactions, where remarkable electrochemical properties with a specific capacity of 285 mAh g⁻¹ after the 1000th cycling test. The MnO nanoparticles with fluorine-doped carbon had 40 mAh g⁻¹ after 200 cycles.

Above noted all capacitor material showed good conductivity, high energy and high safety. According to the above-mentioned articles, the specific capacitance of each sample was less than that of our prepared Mn-doped high surface area of activated carbon. Furthermore, the charge-transfer properties of the above samples had much less than the Mn-doped HSAC because of the big semicircle in the Nyquist plot. The Mn-doped high surface of activated carbon had stable energy density and superior cycling stability that were demonstrated in our supercapacitor system.

Conclusion

In summary, the positive electrode was prepared by means of the Mn-doped high surface area of activated carbon (HSAC), and LaNi₅ was used for the negative electrode. The prominent rate capability of the Mn-doped MnYP-600HTT and MnYP-00HTT electrode can be ascribed to the unique structure, in which HSAC formed connections with Mn. The special-structured active material increased the redox-reaction rate, contact area between electrolyte and electrode, it can improve the electrochemical performance of the material. Clearly, Mn-doped MnYP-600HTT and MnYP-800HTT can achieve both relatively high specific capacity and good cycling behavior, simultaneously. The specific capacity of Mn-doped MnYP-600HTT was 262.8 mAh/g, and Mn-doped MnYP-800HTT had 231.1 mAh/g at the 1st cycle. After the 500th cycle, the specific capacities were decreased to 165.0 and 161.6 mAh/g, respectively. The specific surface area of MnYP-800HTT was higher than that of MnYP-600HTT, and the Mn amount in MnYP-600HTT was 47.22%, and in MnYP-800HTT was 2.98%. The Mn-amount can affect the surface of HSAC and change the electrochemical property. The Mn-doped high

surface of activated carbon had stable energy density and superior cycling stability as were demonstrated in our supercapacitor system.

Received: 7 September 2020; Accepted: 26 October 2020

Published online: 12 January 2021

References

- Kang, K. & Ceder, G. Battery materials for ultrafast charging and discharging. *Nature* **458**, 190–193 (2009).
- Yang, C. C., Sun, W. C., Kumar, A., Pattanayak, B. & Tseng, T. Y. Templating synthesis of nickel cobaltite nanoflakes and their nanocomposites for making high-performance symmetric supercapacitors. *Mater. Today Energy* **14**, 100356 (2019).
- Simon, P., Gogotsi, Y. Materials for electrochemical capacitors, nanoscience and technology: A collection of reviews from nature journals. *World Sci.* 320–329 (2010).
- Jiang, W. *et al.* Ternary hybrids of amorphous nickel hydroxide–carbon nanotube–conducting polymer for supercapacitors with high energy density, excellent rate capability, and long cycle life. *Adv. Funct. Mater.* **25**, 1063–1073 (2015).
- He, G. *et al.* Self-standing electrodes with core-shell structures for high-performance supercapacitors. *Energy Stor. Mater.* **9**, 119–125 (2017).
- Zhou, S. Z., Zhou, G. Y., Jiang, S. H., Fan, P. C. & Hou, H. Q. Flexible and refractory tantalum carbide-carbon electro spun nanofibers with high modulus and electric conductivity. *Mater. Lett.* **200**, 97–100 (2017).
- Chen, D., Hu, X., Huang, Y., Qian, Y. & Li, D. Facile fabrication of nanoporous BCN with excellent charge/discharge cycle stability for high-performance supercapacitors. *Mater. Lett.* **246**, 28–31 (2019).
- Wang, Y. C. *et al.* Reduced mesoporous Co₃O₄ nanowires as efficient water oxidation electrocatalysts and supercapacitor electrodes. *Adv. Energy Mater.* **4**, 1400696 (2014).
- Yu, M. H. *et al.* Valence-optimized vanadium oxide supercapacitor electrodes exhibit ultrahigh capacitance and super-long cyclic durability of 100,000 cycles. *Adv. Funct. Mater.* **25**, 3534–3540 (2015).
- Ji, H. M. *et al.* In situ preparation of sandwich MoO₃/C hybrid nanostructures for high-rate and ultralonglife supercapacitors. *Adv. Funct. Mater.* **25**, 1886–1894 (2015).
- Ko, W. Y., Liu, Y. C., Lai, J. Y., Chuang, C. C. & Lin, K. J. The effect of EV aggregators with time-varying delays on the stability of a load frequency control system. *ACS Sustain. Chem. Eng.* **7**, 669–678 (2018).
- Cho, Y., Oh, P. & Cho, J. A new type of protective surface layer for high-capacity Ni-based cathode materials: nano scaled surface pillaring layer. *Nano Lett.* **13**, 1145 (2013).
- Sun, Y. K., Lee, D. J., Lee, Y. J., Chen, Z. & Myung, S. T. Cobalt-free nickel rich layered oxide cathodes for lithium-ion batteries. *ACS Appl. Mater. Interfaces* **5**, 11434 (2013).
- Warren, R., Sammoura, F., Tounsi, F., Sanghadasa, M. & Lin, L. Highly active ruthenium oxide coating via ALD and electrochemical activation in supercapacitor applications. *J. Mater. Chem. A* **3**, 15568–15575 (2015).
- Kim, S. I., Lee, J. S., Ahn, H. J., Song, H. K. & Jang, J. H. Facile route to an efficient NiO supercapacitor with a three-dimensional nanonetwork morphology. *ACS Appl. Mater. Interfaces* **5**, 1596–1603 (2013).
- Lai, C., Sun, Y. & Lin, B. Synthesis of sandwich-like porous nanostructure of supercapacitors. *Mater. Today Energy* **13**, 342–352 (2019).
- Gopi, C. V. M. *et al.* One-pot synthesis of copper oxide–cobalt oxide core–shell nano cactus-like heterostructures as binder-free electrode materials for high-rate hybrid supercapacitors. *Mater. Today Energy* **14**, 100358 (2019).
- Yu, G. *et al.* Enhancing the supercapacitor performance of graphene/MnO₂ nanostructured electrodes by conductive wrapping. *Nano Lett.* **11**, 4438–4442 (2011).
- Yuan, C. *et al.* Ultrathin mesoporous NiCo₂O₄ nanosheets supported on Ni foam as advanced electrodes for supercapacitors. *Adv. Funct. Mater.* **22**, 4592–4597 (2012).
- Zhang, J., Chen, Z., Wang, Y. & Li, H. Morphology-controllable synthesis of 3D CoNiO₂ nano-networks as a high-performance positive electrode material for supercapacitors. *Energy* **113**, 943–948 (2016).
- Wei, Q. *et al.* Sodium ion capacitor using pseudocapacitive layered ferric vanadate nanosheets cathode. *iScience* **6**, 212–221 (2018).
- Liu, C. *et al.* High energy and power lithium-ion capacitors based on Mn₂O₄/3D-graphene as anode and activated polyaniline-derived carbon nanorods as cathode. *Chem. Eng. J.* **370**, 1485–1492 (2019).
- Zhang, J. *et al.* Hierarchical Mn-doped Fe₂O₃@rGO hollow core-shell spheres for high-performance hybrid capacitor. *Mater. Today Energy* **17**, 100388 (2020).
- Chen, L. *et al.* Integrated nanocomposite of LiMn₂O₄/graphene/carbon nanotubes with pseudocapacitive properties as superior cathode for aqueous hybrid capacitors. *J. Electroanal. Chem.* **842**, 74–81 (2019).
- Ifitkhar, H., Debananda, M., Ganesh, D., Charmaine, L., Saad, G.M., Mostafa, S.S., Jae, J.S. Different controlled nanostructures of Mn-doped ZnS for high-performance supercapacitor applications. *J. Energy Storage*, **32**, 101767 (2020).
- Teeparthi, S. R., Awin, E. W. & Kumar, R. Dominating role of crystal structure over defect chemistry in black and white zirconia on visible light photocatalytic activity. *Sci. Rep.* **8**, 5541 (2018).
- Hui, L., Shuang, L., Zhiling, Z., Xiaonan, Ali, A., Nguyen, D. C. T., Cho, K. Y., Oh, W. C. A simple ultrasonic-synthetic route of Cu₂Se-graphene-TiO₂ ternary composites for carbon dioxide conversion processes, *Fullerenes Nanotubes Carbon Nanostruct.* **26**(12), 827–836 (2018).
- Navi 'o, J.A., Hidalgo, M.C., Colo 'n, G., Botta, S.G., Litter, M.I. Preparation and physicochemical properties of ZrO₂ and Fe/ZrO₂ prepared by a sol-gel technique, *Langmuir* **17**, 202–210 (2001).
- Wang, Y. *et al.* A reduced graphene oxide/mixed-valence manganese oxide composite electrode for tailorable and surface mountable supercapacitors with high capacitance and super-long life. *Energy Environ. Sci.* **10**, 941–949 (2017).
- Qu, D. *et al.* Synthesis of MnO nano-particle@Flourine doped carbon and its application in hybrid supercapacitor. *Appl. Surf. Sci.* **413**, 344–350 (2017).
- Xi, Z. *et al.* Bamboo-like composites of V₂O₅/polyindole and activated carbon cloth as electrodes for all-solid-state flexible asymmetric supercapacitors. *ACS Appl. Mater. Interfaces* **8**, 3776–3783 (2016).
- Shengyang, D. *et al.* Flexible sodium-ion pseudocapacitors based on 3D Na₂Ti₃O₇ nanosheet arrays/carbon textiles anodes. *Adv. Funct. Mater.* **26**, 3703–3710 (2016).
- Jing, Z. *et al.* Growing NiS₂ nanosheets on porous carbon microtubes for hybrid sodium-ion capacitors. *J. Power Sources* **451**, 227737 (2020).

Acknowledgements

This research was supported by the Korean Electrotechnology Research Institute (KERI) primary research program through the National Research Council of Science and Technology (NST) funded by the Ministry of Science, ICT (MSIT) (No. 20A01029).

Author contributions

W.C.O. planned the research, and S.Y., I.J.K., M.C. Kim and S.E.S. analyzed samples in South Korea. O.Z. and K.N.F. wrote the manuscript.

Competing interests

The authors declare no competing interests.

Additional information

Correspondence and requests for materials should be addressed to S.E.S. or W.-C.O.

Reprints and permissions information is available at www.nature.com/reprints.

Publisher's note Springer Nature remains neutral with regard to jurisdictional claims in published maps and institutional affiliations.



Open Access This article is licensed under a Creative Commons Attribution 4.0 International License, which permits use, sharing, adaptation, distribution and reproduction in any medium or format, as long as you give appropriate credit to the original author(s) and the source, provide a link to the Creative Commons licence, and indicate if changes were made. The images or other third party material in this article are included in the article's Creative Commons licence, unless indicated otherwise in a credit line to the material. If material is not included in the article's Creative Commons licence and your intended use is not permitted by statutory regulation or exceeds the permitted use, you will need to obtain permission directly from the copyright holder. To view a copy of this licence, visit <http://creativecommons.org/licenses/by/4.0/>.

© The Author(s) 2021